Numerical Heat Transfer, Part A: Applications: An International Journal of Computation and Methodology
Publication details, including instructions for authors and subscription information:
http://www.tandfonline.com/loi/unht20

ANALYSIS OF THE FLOW IN THE GROOVES OF A MOLECULAR PUMP

Yeng-Yung Tsui, Chia-Ping Kung, Hong-Ping Cheng
Published online: 29 Oct 2010.

To cite this article: Yeng-Yung Tsui, Chia-Ping Kung, Hong-Ping Cheng (2001) ANALYSIS OF THE FLOW IN THE GROOVES OF A MOLECULAR PUMP, Numerical Heat Transfer, Part A: Applications: An International Journal of Computation and Methodology, 40:1, 73-88, DOI: 10.1080/10407780121549

To link to this article: http://dx.doi.org/10.1080/10407780121549

Numerical Heat Transfer, Part A, 40:73–88, 2001

1040-7782/01 $12.00 + .00

ANALYSIS OF THE FLOW IN THE GROOVES OF A MOLECULAR PUMP

Yeng-Yung Tsui and Chia-Ping Kung
Department of Mechanical Engineering, National Chiao Tung University, Hsinchu 300, Taiwan, Republic of China

Hong-Ping Cheng
Precision Instrument Development Center, Hsinchu 300, Taiwan, Republic of China

A computational procedure used to solve conservation equations governing the slip flow in a molecular pump of the Holweck type is developed. The finite volume method is used for discretization and the grid is arranged in the curvilinear, nonstaggered form. The slip boundary condition is imposed on the solid walls. The clearance gap between the rotor and the casing is ignored. It is evident from the calculation that the pressure difference between the two side walls of the channel, termed pressure side and suction side, varies in accordance with the pressure difference between the inlet and the outlet of the pump. Thus, the side-wall pressure difference can play the role of an indicator of pumping effectiveness. Tests on a variety of configurations show that to achieve the best performance both the spiral angle and the channel height need to be optimized. Besides, it is better to have fewer flow channels and to place these channels on the rotor instead of on the casing.

INTRODUCTION

The development of the molecular pump dates back to the early 1900s. The first pump of this type was introduced by Gaede [1] using a series of parallel grooves around the circumference of a rotor. Later, spiral grooves were mounted either on a rotating cylinder by Holweck [2] or on a rotating disc by Siegbahn [3]. These three types of pump are termed the molecular drag pump (MDP). A different design, called the turbomolecular pump (TMP) came from Becker [4], in which the pumping channels are formed by rows of rotating and stationary blades. The MDPs did not draw much attention until recently because of their relatively low pumping speed and questionable reliability during the early days. The TMP has the advantage of high pumping speed and low ultimate pressure. However, the MDP has a high compression ratio and is capable of raising the foreline pressure to the range of

Received 8 January 2001; accepted 24 February 2001.
The authors acknowledge the support provided by the Precision Instrument Development Center of the National Science Council, Republic of China.
Address correspondence to Dr. Y. Y. Tsui, Department of Mechanical Engineering, National Chiao Tung University, 1001 Ta Hsueh Road, Hsinchu, Taiwan 30050, Republic of China.

NOMENCLATURE

A	cross-sectional area	α	channel angle
B_{ij}	diffusion matrix	ϕ	transport entity
f	accommodation coefficient of momentum	λ	mean free path
		μ	dynamic viscosity
h	channel height	μ'	apparent viscosity
J	Jacobian of coordinate transformation	ρ	density
		ξ_i	curvilinear coordinates
K_n	Knudsen number	Ω	angular velocity vector
p	pressure		
r	radial coordinate	**Subscripts**	
$\vec{R}$	position vector	p	value at pressure side
T	temperature	s	value at suction side
U_i	contravariant velocity in the ξ_i direction	w	wall value
		1	value at inlet
$\vec{V}$	flow velocity vector	2	value at exit

1 to 10^3 pa. Therefore, through combination of the TMPs with the MDPs the demanding of high throughputs together with high discharge pressures can be achieved.

The pumping principle of the molecular pumps is based on the occurrence of when gas molecules impinge on a rapidly rotating surface, momentum is imparted to the gas to counterbalance the pressure rise encountered in the flow channel. One way to model the molecular flow in these pumps makes use of the equation given by Gaede in [5–7]. Another approach developed by Kruger and Shapiro [8] uses the Monte Carlo method to calculate the probabilities of molecules passing through the flow channels from both the inlet and the outlet. With these transmission probabilities the maximum compression ratio and pumping speed can be obtained. The above approaches are applicable to the free molecular flow. For the flow in the transition regime the direct simulation Monte Carlo method is the most suitable [9, 10]. As mentioned before, the working pressure for the MDP can be up to 10^3 pa. At these high operation pressures the flow in the pump will reach the continuum regime. Not much effort was devoted to this area in the past. In some research the analysis is based on the superposition of a Poiseuille flow on a Couette flow [6, 11]. Apparently, this simple analytic model cannot fully reflect the real flow in the pump. In this study the full Navier–Stokes equation are solved using a numerical method to investigate the flow behavior in the Holweck-type pump. The flow is in the slip flow regime, and, thus, the slip boundary condition is employed in the calculation.

MATHEMATICAL METHOD

A schematic drawing of the rotor of the Holweck-type molecular pump is illustrated in Figure 1. There are six grooves on the rotor. Because of the periodic arrangement only one groove is considered in the calculation. Because the Reynolds number is less than 20 in the current study, the flow is in the laminar regime. The flow

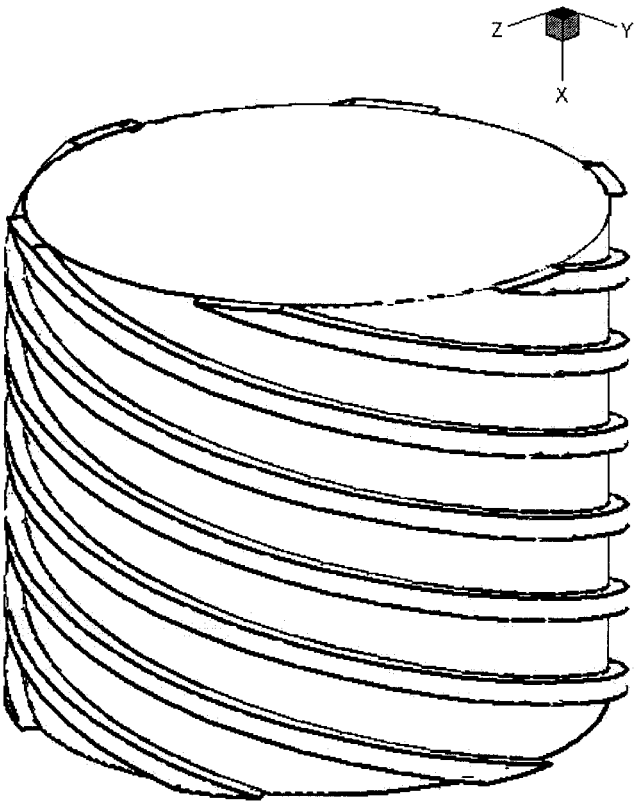

Figure 1. A schematic drawing of the pump.

is assumed to be fixed at the room temperature of 300°K. In the numerical calculation the conservation equations of mass and momentum together with the equation of state are solved. Because the flow grooves are sited on the rotor, a rotating frame of reference is necessary. To cope with the helical geometry of the grooves a transformation from the cylindrical coordinates to the curvilinear coordinates is undertaken. Then the governing equations can be written in the following form:

$$\frac{1}{Jr}\ \frac{\partial}{\partial \xi_i}(\rho U_i \phi) = \frac{1}{Jr}\ \frac{\partial}{\partial \xi_i}\left[\frac{\mu}{Jr}\left(B_{ij}\frac{\partial \phi}{\partial \xi_j}\right)\right] + S_\phi \tag{1}$$

where ϕ stands for the velocity components in the cylindrical coordinates, and B_{ij} represents the diffusion matrix. For details of this matrix, see Tsui and colleagues [12]. The rotation of the frame gives rise to centrifugal force and Coriolis force, which are absorbed in the source term S_ϕ.

$$\vec{F} = -2\rho\vec{\Omega} \times \vec{V} + \rho\vec{\Omega} \times (\vec{\Omega} \times \vec{R}) \tag{2}$$

From gas kinetics it can be shown that the mean free path of gas molecules λ is related to the pressure and temperature as

$$\frac{\lambda P}{T} = \text{const} \tag{3}$$

The discharge pressure of the pump of the current study is fixed at 133 pa (= 1 torr). According to the above relation, the mean free path is around 0.05 mm. The Knudsen number, $K_n = \lambda/h$, where h is the height of the flow channel (= 4.06 mm), is around 0.01. Therefore, the flow field will cover the slip flow regime. The slip flow at the solid wall is most commonly given as

$$V_o = V_w + \frac{2-f}{f}\lambda\left(\frac{dV}{dy}\right)_w \tag{4}$$

where V_o is the flow velocity at the wall, V_w is the velocity of the solid wall itself, and f is the accommodation coefficient of momentum. The accommodation coefficient usually takes a value close to 1. In the current calculation the value of unity is adopted.

The governing equations shown in Eq. (1) are of divergence form. By applying the Gauss theorem of divergence, we can transform volume integral of the equation to a surface integral. Then the task of discretization can be accomplished via suitable evaluation of the covective and diffusive fluxes. Convection terms are approximated by the second-order linear upwind difference [13], whereas the diffusion terms are approximated by the central difference. The grids used are arranged in the nonstaggered manner; that is all dependent variables are collocated at the cell center. To avoid the pressure-velocity decoupling caused by the nonstaggered grid arrangement, a special interpolation practice [14] is utilized to calculate the mass flux through each cell face. By forcing the mass fluxes to satisfy the continuity constraint a pressure-correction equation is obtained. An iterative solution procedure can then be employed.

The implementation of the slip boundary condition deserves a discussion. A drawing of a control volume adjacent to a solid wall is given in Figure 2. The shear stress at the wall can be calculated as

$$\tau = \mu\left(\frac{dV}{dy}\right)_w = \mu\frac{V_p - V_o}{\delta n} \tag{5}$$

where δn is the normal distance form the point p to the wall. The gas velocity at the wall can be approximated as

$$V_o = V_w + \frac{2-f}{f}\,\lambda\frac{V_p - V_o}{\delta n} \tag{6}$$

A direct way to implement the boundary condition can be obtained via successive substitution of V_o given by the above equation into Eq. (5) during the solution iteration. However, in this manner the solution procedure is not easy to converge because the velocity V_o on the right-hand side of Eq. (6) lags by one iteration.

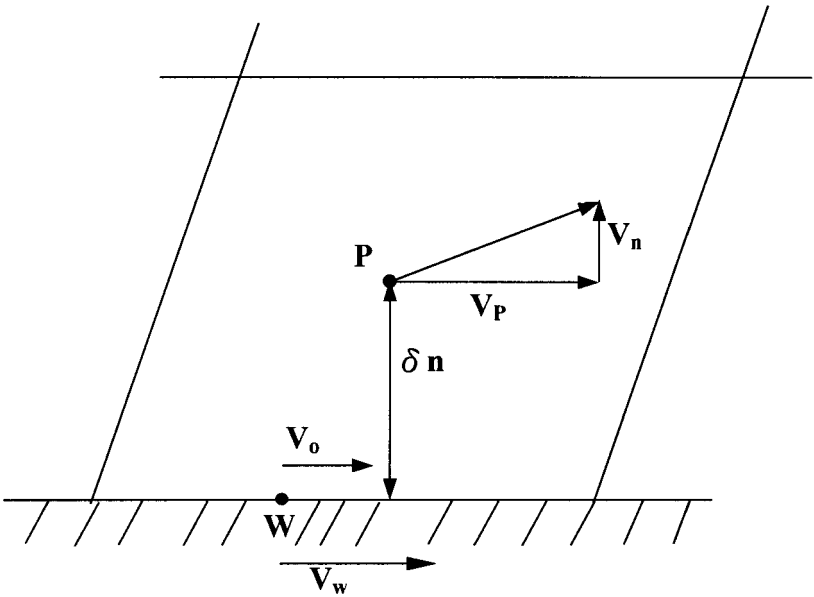

Figure 2. Illustration of a control volume near the wall.

A better way is given as follows. Because

$$V_p - V_o = \frac{(V_p - V_w)}{(1 + (2 - f)/f(\lambda/\delta n))} \tag{7}$$

the shear stress can be calculated from

$$\tau = \mu' \frac{V_p - V_w}{\delta n} \tag{8}$$

Here μ' stands for an apparent viscosity:

$$\mu' = \frac{\mu}{1 + (2 - f)/f(\lambda/\delta n)} \tag{9}$$

RESULTS AND DISCUSSION

In the current study the baseline configuration of the pump considered is the same as that used by Nanbu and Igarashi [15]. However, in the calculation of Nanbu and Igarashi's configuration the flow channel was treated as a rectangular channel and a stationary frame was used. The axial length of the pump is 53.5 mm while the outer diameter of the rotor is 137.6 mm. There are six spiral channels on the rotor. The width and height of each channel are 53.5 mm and 4.06 mm. The spiral angle of the channel is 15°. The clearance between the casing and the rotor is ignored. The rotor rotates at 18000 rpm. Nitrogen is used as the working fluid.

The pumping process is assumed to be isothermal at 300°K. The outlet pressure is maintained at a fixed level of 133 pa and a number of mass flow rates, 300 sccm, 600 sccm, 960 sccm, and 1440 sccm, are under consideration. Three different levels of grid, 52*22*12, 102*32*22, and 132*52*32 have been tested to exam grid sensitivity. A typical grid is illustrated in Figure 3. The differences in the resulting pressure distribution are insignificant. Thus, the second level of mesh is used in the following.

To illustrate flow structure the contours of the axial velocity and the transverse velocity vectors at $x/L = 0.6$ and 1 for 300 sccm and 960 sccm are shown in Figures 4 and 5. Here L stands for the total length of the flow channel. For the low flow rate reverse flow forms at the two side walls in the lower half of the channel. The strength of the reverse flow decreases as the flow rate increases because the adverse pressure gradient prevailing in the pump is reduced accordingly, which will be clear in the following. Because of the moving wall at the top the transverse flow behaves like a Couette flow. However, as seen from Figure 4, the flow pattern is transformed to a cavity flow when reverse flow takes place near the bottom wall at the low flow rate.

The variation of the pressure, averaged over the transverse plane, is shown in Figure 6. In this figure and the following P_1 and P_2 denote the pressures at the inlet and the outlet, respectively. It is seen that the pressure rise across the pump increases as the flow rate decreases. For the flow rate of 1440 sccm the pressure decreases monotonically. This indicates that the molecular pump is effective at low pressures. Two sets of results are presented in the figure: one for the use of the slip boundary condition and the other for that of the no-slip boundary condition. For the low flow rate cases the pressure rise is higher for the no-slip flow. The cause of this result is ascribed to more momentum being exerted from the moving surface to the gas as the no-slip boundary condition is being applied.

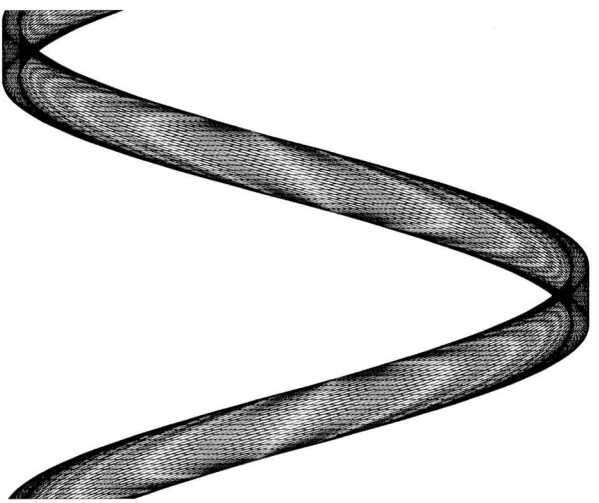

Figure 3. A typical grid arrangement.

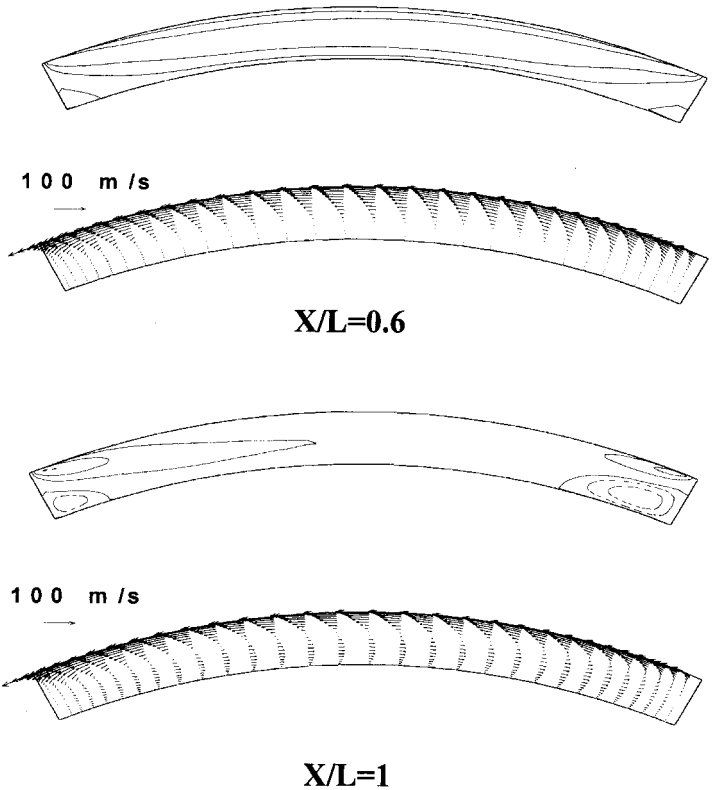

Figure 4. Axial velocity contours and secondary velocity vectors at $x/L = 0.6$ and 1 for 300 sccm. The solid lines represent 5, 10, 15, 20 m/s and the dashed lines -1, -2 m/s.

A comparison of the current predictions with the experimental data [15] is given in Figure 7. Both results indicate a linear decrease of the pressure rise with the flow rate. However, the pressure rise is overpredicted for the low flow rates. This is believed to be the case because the clearance gap between the rotor and the pump casing is not accounted for in the calculation. To illustrate this point Figure 8 is presented. This figure shows the pressure distribution in a plane at the midheight of the channel. Evidently, there exists a pressure difference between the two side walls. As will be seen in the analysis given below, the pressure rise across the channel is reflected by this side-wall pressure difference. Because the clearance gap connects the two side walls of the channel, it is expected that the side-wall pressure difference should decrease and the pumping effectiveness deteriorates accordingly.

A schematic drawing of the spiral channel is shown in Figure 9, in which the channel is straightened, but with an angle α with respect to the circumferential direction. The side with higher pressure P_p is termed the pressure side and the other one with P_s is the suction side. The pressure side is located at the upstream side of the rotation. A force balance over the entire flow channel in the axial direction

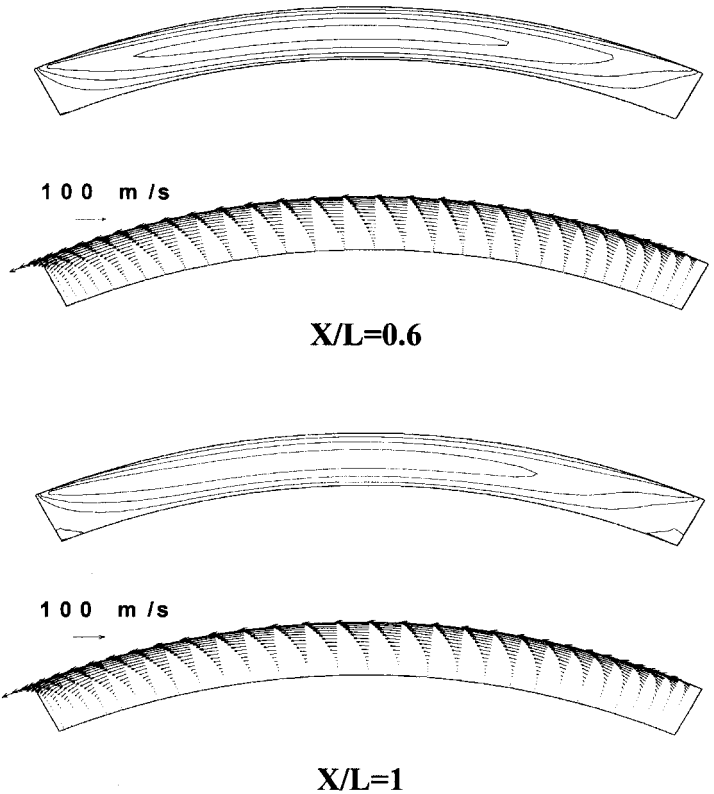

Figure 5. Axial velocity contours and secondary velocity vectors at $x/L = 0.6$ and 1 for 960 sccm. The solid lines represent 5, 10, 15, 20 m/s and the dashed lines -1, -2 m/s.

is constructed:

$$(P_2 - P_1)A \approx (P_p - P_s)A_w \cos\alpha - F_x \tag{10}$$

Here A and A_w designate the cross-sectional area of the channel and the side-wall area, respectively, and F_x represents the total frictional force exerted by the solid walls in the axial direction. In the above equation the difference between the inlet and outgoing momentum fluxes is ignored. It is clear from this equation that the pressure difference between the pressure and the suction sides brings about the pressure rise across the channel.

In Table 1 all the terms shown in Eq. (10) together with the average pressures P_p and P_s are listed. As the flow rate increases, the pressure difference between the side walls decreases while the frictional force increases. This results in diminished pressure rise across the pump. Thus, the side-wall pressure difference can be used as an indicator of the effectiveness of the pumping process.

In the following the pump configuration is modified to examine its effects on the pumping performance.

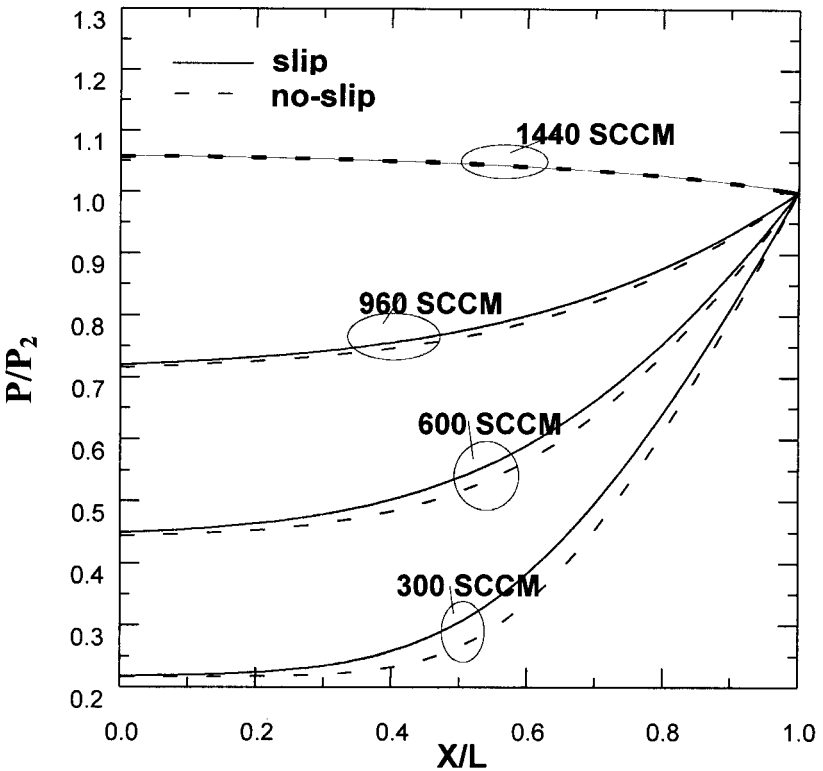

Figure 6. Pressure variation along the channel.

Test of Spiral Angle

The baseline spiral angle α is 15°. In this test the angle varies from 13° to 30° together with a special case of 90°. The resulted pressure variation along the flow channel for 600 sccm is shown in Figure 10. It is evident that the pressure rise across the channel increases with the spiral angle until $\alpha = 25°$, followed by a decrease thereafter. It can be seen from Table 2 that the side-wall pressure difference increases monotonically with the spiral angle. However, it is noted that this pressure difference is multiplied by $\cos\alpha$ in Eq. (10). The value of $\cos\alpha$ decreases as the angle increases. Therefore, there exists an optimum value of α. It can also be seen from Figure 10 that the adverse pressure gradient is high in the inlet region for large angles and high in the exit region for small angles. As a consequence, a better design of the channel is to have larger spiral angles at inlet and smaller angles at outlet.

Test of Channel Height

To examine the influence of channel height three values of height, 3.5 mm, 4.5 mm, and 6 mm, together with the original height 4.06 mm, are under consid-

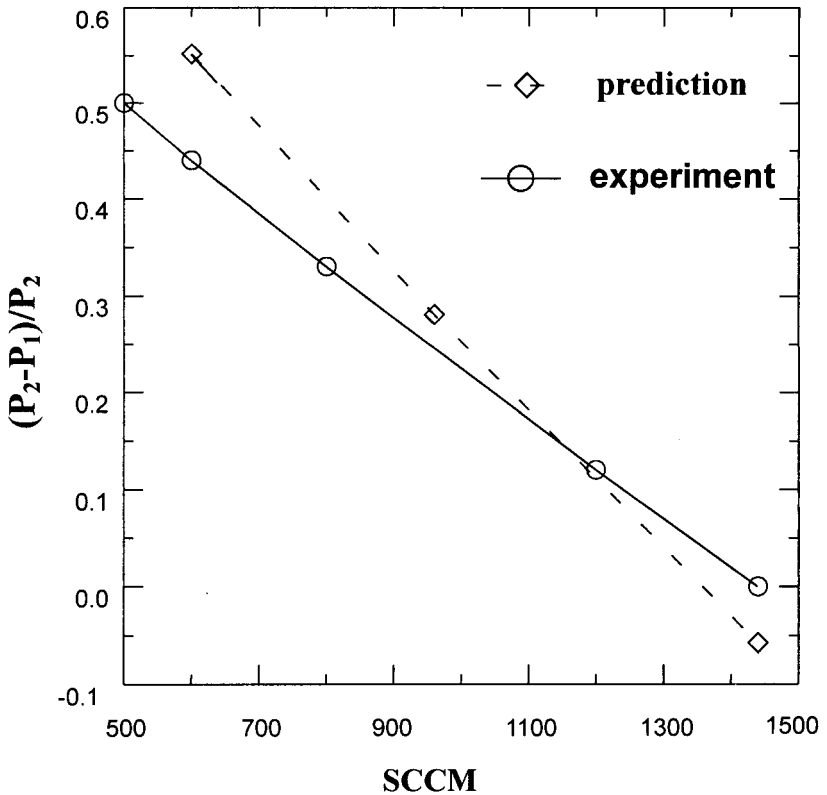

Figure 7. Comparison of the pressure rise with measurements.

eration. It is revealed from Figure 11 for 600 sccm that the pumping performance is enhanced when the channel height is increased up to 4.5 mm, followed by a decrease for the height of 6 mm. The cause of this phenomenon is clear from the following discussion. When the channel height is increased, the cross-sectional area A increases accordingly and the flow velocity is reduced because the flow rate remains as a constant. Thus, more momentum is transferred from the moving wall to the gas for the large height cases. In addition, less frictional force is caused at the stationary walls in spite of the increase of the side-wall area. This results in better pumping effectiveness. However, it should be understood that with a large channel height the strength of the reverse flow is stronger, which leads to a greater pressure loss. Examination of the variation of pressure gradient reveals that a better performance can be obtained by having a taper channel: larger height at outlet and smaller height at outlet.

Test of Channel Number

The numbers of flow channels tested are 4, 6, and 8. Figure 12 reveals that the pumping performance is improved as the channel number decreases. From

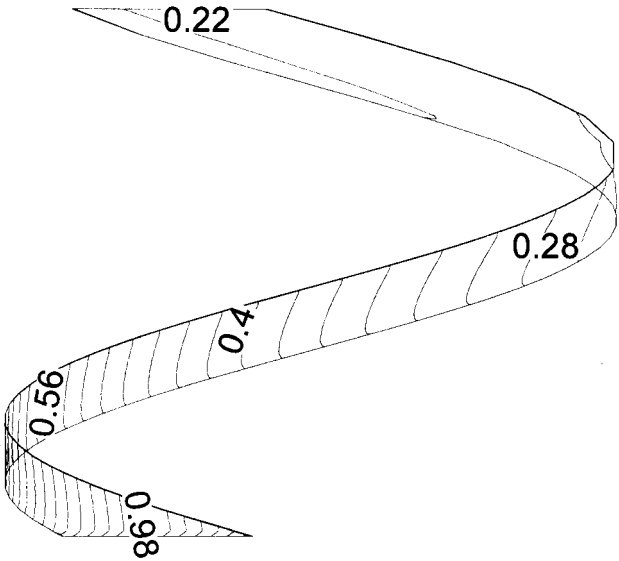

Figure 8. Pressure distribution in a plane near the midheight of the channel.

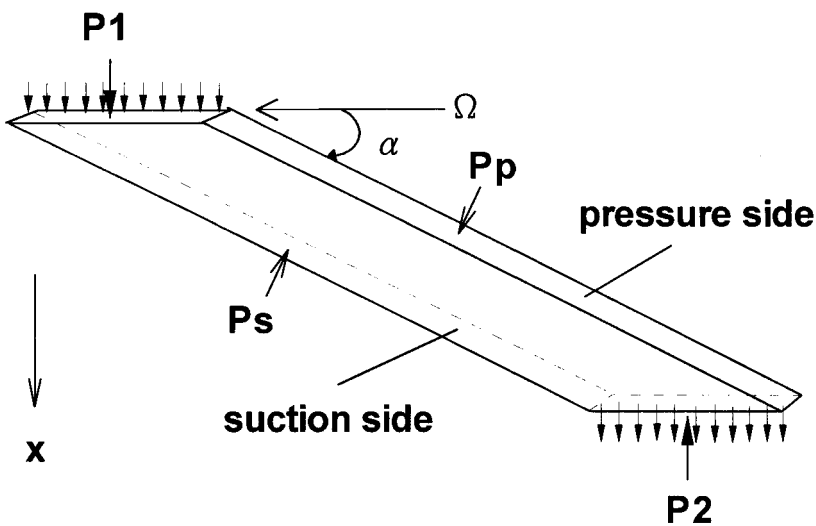

Figure 9. Illustration of the force balance over the entire flow channel.

Table 3 for 600 sccm it is detected that the pressure at the pressure side remains almost constant, but the pressure at the suction side decreases with the channel number. The decrease of channel number brings about wider channel space, which allows a larger pressure difference to form between the side walls by the Couette-like flow.

Table 1. Force balance for various flow rates

	300 sccm	600 sccm	960 sccm	1440 sccm
P_1A (nt)	$6.13*10^{-3}$	$1.24*10^{-2}$	$1.98*10^{-2}$	$2.89*10^{-2}$
P_2A (nt)	$2.75*10^{-2}$	$2.75*10^{-2}$	$2.74*10^{-2}$	$2.73*10^{-2}$
P_pA_w (nt)	$1.13*10^{-1}$	$1.53*10^{-1}$	$1.96*10^{-1}$	$2.46*10^{-1}$
P_sA_w (nt)	$8.62*10^{-2}$	$1.32*10^{-1}$	$1.82*10^{-1}$	$2.42*10^{-1}$
F_x (nt/m^2)	$3.73*10^{-3}$	$4.79*10^{-3}$	$5.65*10^{-3}$	$6.56*10^{-3}$
P_p (nt/m^2)	64.0	87.1	111.6	140.1
P_s (nt/m^2)	49.2	75.4	103.6	137.8

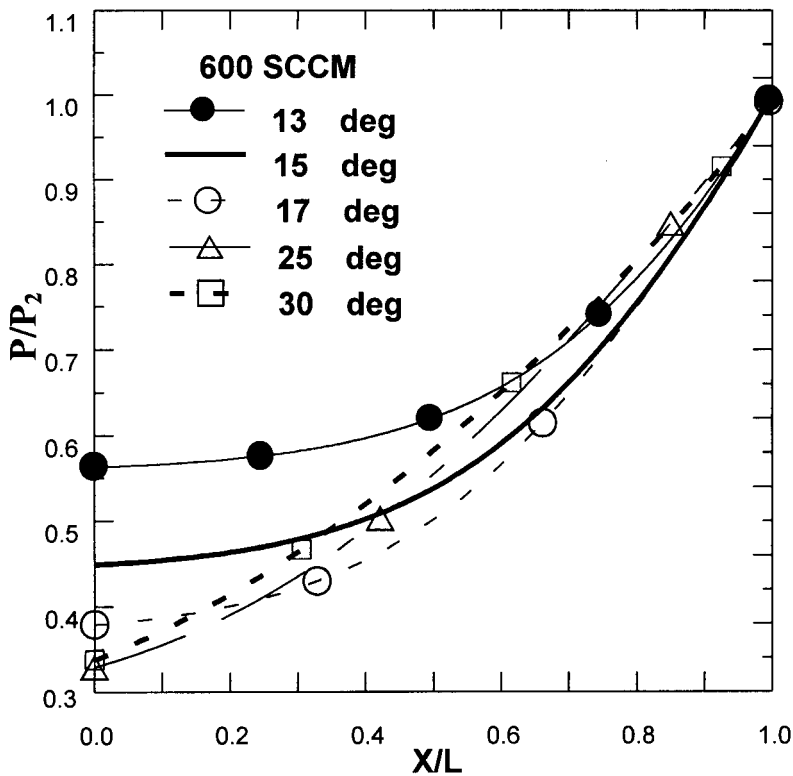

Figure 10. Pressure variation for various spiral angles.

Comparison of the Channels Fixed on the Rotor and the Casing

In the above results the flow channels are placed on the rotor. Another common practice is to place the channels on the casing. Figure 13 indicates that better per-

Table 2. Pressures at the pressure side and suction side for various spiral angles

	15°	25°	30°	90°
P_p (nt/m^2)	87.1	91.9	97.2	164
P_s (nt/m^2)	75.4	68.3	68.5	118.2

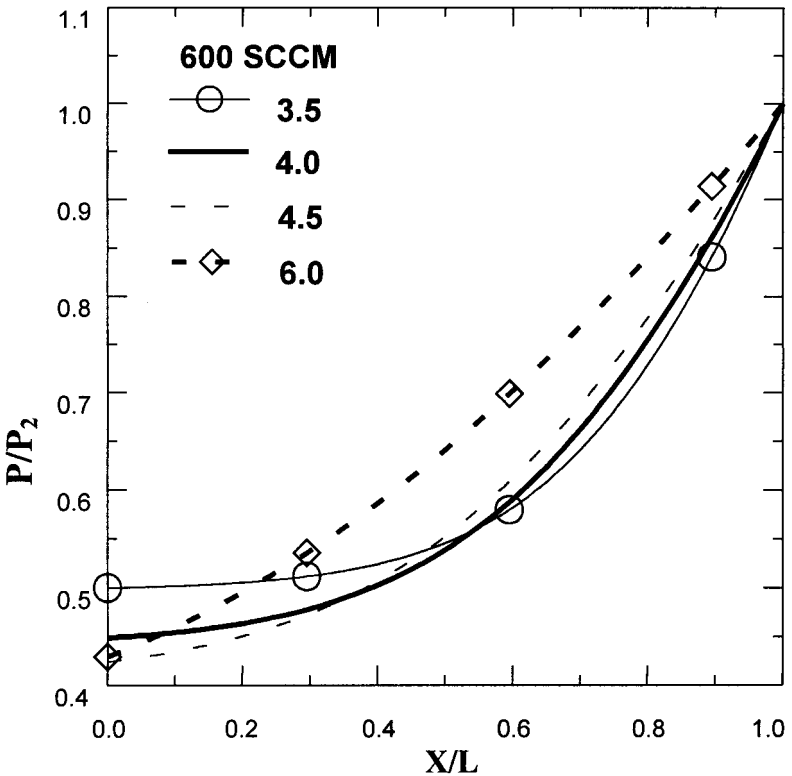

Figure 11. Pressure variation for various channel heights.

formance is yielded when the channels are fixed on the rotor. This is because the speed of the moving wall is higher for this arrangement.

CONCLUSIONS

A three-dimensional numerical analysis model has been successfully developed and applied to examine the flow in a molecular drag pump of Holweck type. The main findings are given in the following.

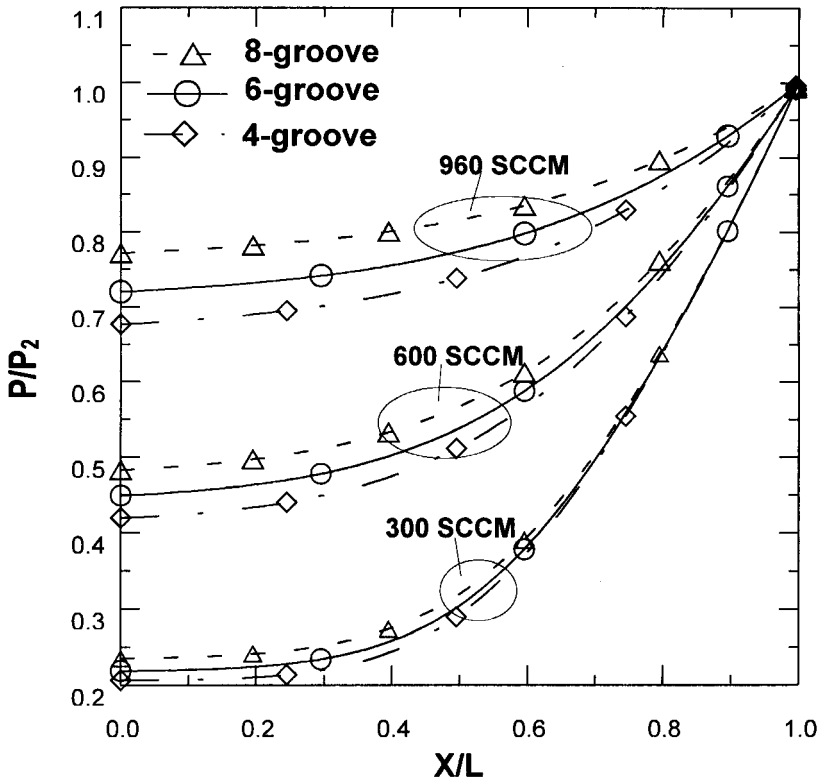

Figure 12. Pressure variation for various channel numbers.

1. From the analysis it is clear that the pressure rise across the channel can be attributed to the difference between the pressure side and the suction side of the channel.
2. The increase of the spiral angle brings about an increase of the side-wall pressure difference. But the component of this pressure difference in the axial direction decreases with the angle. As a consequence, there exists an optimum value of spiral angle.

Table 3. Pressures at the pressure side and suction side for various channel numbers

	4-groove	6-groove	8-groove
P_p (nt/m^2)	87.8	87.1	88.6
P_s (nt/m^2)	69.9	75.4	80.0

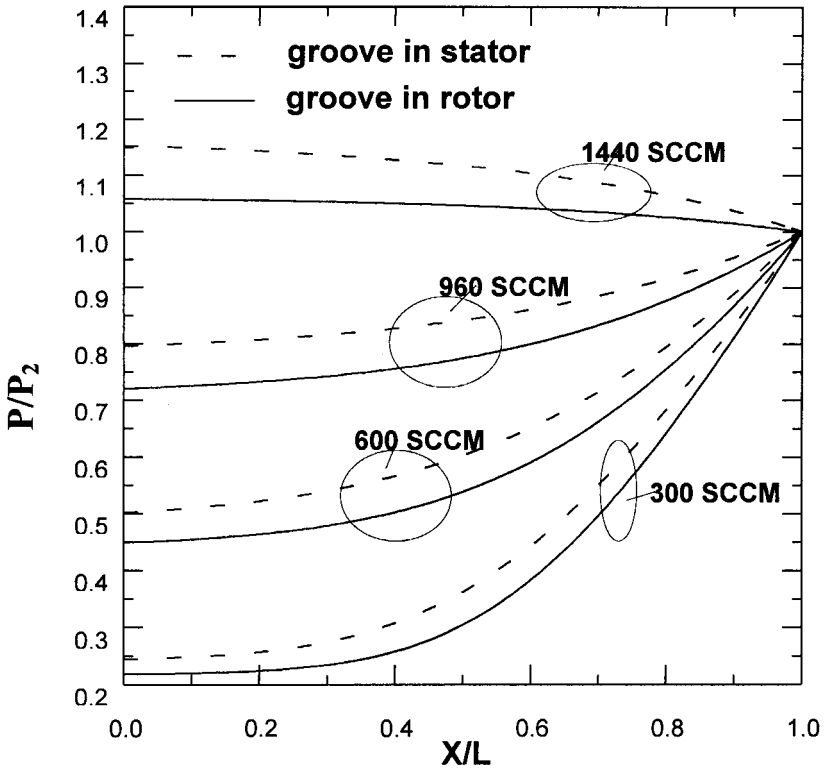

Figure 13. Pressure variation for the placement of the channel on the rotor and on the casing.

3. The increase of the channel height leads to more momentum being transferred from the moving surface to the gas because the speed of the gas becomes lower. However, it induces stronger reverse flow. Therefore, the channel height also needs to be optimized. The pressure variation indicates that a better design is to have larger spiral angle and channel height at inlet and smaller spiral angle and height at outlet.
4. When the channel number increases, the spacing between side walls decreases, causing a decrease in the side-pressure difference as well as the pressure rise across the channel.
5. Compared with the placement of the channels on the rotor, the speed of the moving surface is lower as the channels are sited on the casing. It gives rise to lower pumping performance.

REFERENCES

1. W. Gaede, Die Molekularluftpumpe, *Annalen der Physik*, vol. 41, pp. 337–380, 1913.
2. F. Holweck, Pompe Moleculaire Helicoidale, *C. R. Acad. Sci.*, vol. 43, p. 177, 1923.
3. M. Siegbahn, A New Design for a High Vacuum Pump, *Ark. Math. Astron. Phys.*, vol. 30b, pp. 261–270, 1943.

4. W. Becker, Eine Neue Molekularpumpe, *Vakuum Technik*, vol. 7, p. 49, 1958.
5. W. Becker, The Turbomolecular Pump, Its Design, Operation and Theory: Calculation of the Pumping Speed for Various Gases and Their Dependence on the Forepump, *Vacuum*, vol. 16, pp. 625–632, 1966.
6. C. N. Panos, A. G. Antoniou, and S. E. Valamontes, The Helicoid Multi-Groove Vacuum Pump in Both Viscous and Molecular States, *Vacuum*, vol. 45, pp. 841–847, 1994.
7. A. G. Antoniou, S. E. Valamontes, C. N. Panos, and E. S. Valamontes, The Turbomolecular Pump in Molecular State, *Vacuum*, vol. 46, pp. 709–715, 1995.
8. C. H. Kruger and A. H. Shapiro, Vacuum Pumping with a Bladed Axial-Flow Turbo-Machine, 7th Nat. Symp. Vac. Techn. Transaqct., pp. 6–12, 1960.
9. G. A. Bird, *Molecular Gas Dynamics and the Direct Simulation of Gas Flows*, Clarendon Press, Oxford, 1994.
10. Y. K. Lee and J. W. Lee, Direct Simulation of Compression Characteristics for a Simple Drag Pump Model, *Vacuum*, vol. 47, pp. 807–809, 1996.
11. M. Spanol, R. Cerruti, and J. Helmer, Turbomolecular Pump Design for High Pressure Operation, *J. Vac. Sci. Technol.*, vol. A16, pp. 1151–1156, 1998.
12. Y.-Y. Tsui, P.-W. Wu, and C.-W. Liao, Flow Modeling in Turbofan Mixing Duct, *Numer. Heat Transfer, Part A*, vol. 26, pp. 219–236, 1994.
13. Y. Y. Tsui, A Study of Upstream-Weighted High-Order Differencing for Approximation to Flow Convection, *Int. J. Numer. Methods Fluids*, vol. 13, pp. 167–199, 1991.
14. C. M. Rhie and W. L. Chow, A Numerical Study of the Turbulent Flow Past an Isolated Airfoil with Trailing Edge Separation, *AIAA J.*, vol. 21, pp. 1525–1532, 1983.
15. K. Nanbu and S. Igarashi, Three-Dimensional Low-Density Flows in the Spiral Grooves of a Turbo-Molecular Pump, *Computers Fluids*, vol. 21, pp. 221–228, 1992.